

Proceedings of the International Symposium on Physics of Materials (ISPMA 14), September 10–15, 2017, Prague

High Temperature Mechanical Properties and Microstructure of Ti–Nb–Zr–Ta–O Biomedical Alloy

D. PREISLER^{a,*}, J. STRÁSKÝ^a, P. HARCUBA^a, F.G. WARCHOMICKA^b AND M. JANEČEK^a

^aCharles University, Department of Physics of Materials, Ke Karlovu 5, 121 16 Prague, Czech Republic

^bGraz University of Technology, Institute of Materials Science and Welding, Kopernikusgasse 24/I, Graz, Austria

Sufficient biocompatibility and high strength are fundamental properties required for total joint endoprostheses material. Recently developed Ti-based alloy Ti–35.3Nb–7.3Zr–5.7Ta–0.7O (wt%) exhibits these properties. However, the as-cast material does not meet requirements for fatigue resistance due to pores and very coarse grain structure and therefore a feasible forming procedure must be established. Gleeble apparatus was used to deform the studied alloy at high temperatures (from 800 °C to 1400 °C) and high strain rates (up to 1 s⁻¹) to the total strain of 0.5. Mechanical properties at elevated temperatures were evaluated. The resulting microstructure was investigated by scanning electron microscopy and electron backscatter diffraction (EBSD). It was found that forming procedure should be performed at temperatures higher than 1400 °C to reach conditions similar to forming of Ti–6Al–4V. Calculation of kernel average misorientation from EBSD data showed that most deformation is stored in the material in the vicinity of grain boundaries without any apparent recrystallization.

DOI: [10.12693/APhysPolA.134.636](https://doi.org/10.12693/APhysPolA.134.636)

PACS/topics: 81.05.Bx, 81.40.Lm, 81.70.Bt, 68.37.Hk

1. Introduction

Titanium and its alloys have been traditionally used in medicine and orthopaedics [1, 2]. There are numerous applications where these materials take advantage from excellent corrosion resistance, high biocompatibility and low Young's modulus. Commercially pure Ti has been successfully used as tooth replacement material and $\alpha+\beta$ Ti alloy Ti–6Al–4V (wt%) (Ti64), primarily developed for aerospace industry, has been used for decades as a material for implants of big body joints. Ti64 has a very high strength (around 1000 MPa), but the drawback is the content of toxic vanadium and high Young's modulus (110 GPa [3]) — although very low when compared to steels, it is still much higher than that of a bone (10–30 GPa [4]).

Alloys that retain pure β phase after quenching, which ensures lower Young's modulus [5], and contain only biocompatible elements (Nb, Ta, Mo, Zr) [6] are extensively studied nowadays. Several biocompatible Ti–Nb–Zr–Ta based alloys exhibiting the Young's modulus as low as 50–60 GPa have emerged recently; one of them having the composition Ti–35.3Nb–7.3Zr–5.7Ta (wt%; all composition values are in wt% from now on) [7]. However, their strength is approximately only one half of that of Ti64. Small amount of oxygen addition, typically 0.3%–0.5%, has a great strengthening effect on this type of β -Ti alloys [8–11] and adding more than 0.5% of oxygen, as in Ti–35.3Nb–7.3Zr–5.7Ta–0.7O, yields even higher strength, sharp yield point and deformation strengthening [12, 13]. The addition of 0.7% of oxygen raises Young's modulus to the value of 80 GPa that is still significant improvement to 110 GPa of Ti64.

The alloy with the composition Ti–35.3Nb–7.3Zr–5.7Ta–0.7O, studied in this work, contains very large grains (0.5–3 mm), small pores (5–30 μm) and dendritic inhomogeneities after casting. As a consequence, it exhibits a reduced strength [14] and poor fatigue performance. Forming procedure is therefore necessary. The goal of the current work is to find suitable conditions of working, namely the temperature and the speed of forming to allow its feasible procedure.

2. Material and methods

The alloy used in this study was cast at Retech, Co., USA in helium atmosphere. Rod with diameter 55 mm was produced by plasma arc melting of pure Ti, Nb, Zr, Ta and TiO₂ (for oxygen addition) into small compacts and remelting these compacts into final ingot. Cylindrical samples with the diameter of 8 mm and the length of 12 mm were cut from the cast ingot for compression testing using Gleeble[®] 1500 machine equipped with a servo-hydraulic system. Compression tests were performed at temperatures of 800 °C–1400 °C with strain rates $\dot{\epsilon} = 0.01 \text{ s}^{-1}$ and $\dot{\epsilon} = 1 \text{ s}^{-1}$ up to the total strain of 0.5. Duration of a compression test was 0.5 s and 50 s for high strain rate of $\dot{\epsilon} = 1 \text{ s}^{-1}$ and lower strain rate of $\dot{\epsilon} = 0.01 \text{ s}^{-1}$, respectively. Each sample was heated with the rate of 5 K/s up to the final temperature of deformation. Compressive flow curves were recorded *in situ*. Each sample was immediately water quenched after deformation. The resulting microstructure was studied by scanning electron microscope (SEM) Quanta FEG 200FX equipped with EDAX electron backscatter diffraction (EBSD) detector. Samples for microstructural observations were ground with SiC papers up to the grit of 2400 and polished with Buehler vibratory polisher with alumina 0.3 μm , 0.05 μm (for 8 h each) and colloidal silica (for 3 h) suspensions.

*corresponding author; e-mail: preisler.dalibor@gmail.com

3. Results and discussion

Flow curves from compression tests at elevated temperatures are shown in Fig. 1. It should be noted that curves recorded at high strain rate of $\dot{\epsilon} = 1 \text{ s}^{-1}$ contained artefacts and heavy noise and massive smoothing procedure was employed which resulted in wavy curves (mostly recognizable at temperature $1400 \text{ }^\circ\text{C}$). As expected, lower temperatures and higher strain rates lead to higher compressive strength. The sample deformed at $T = 800 \text{ }^\circ\text{C}$ with $\dot{\epsilon} = 0.01 \text{ s}^{-1}$ exhibits the sharp yield point similarly to the tensile flow curves performed at room temperature [13]. On the other hand, flow curves measured at higher temperatures did not exhibit the sharp yield point because the temperature is sufficiently high to activate diffusion of oxygen in matrix and prevent pinning dislocations by interstitial oxygen atoms. Note that the flow curve at $1100 \text{ }^\circ\text{C}$ with $\dot{\epsilon} = 1 \text{ s}^{-1}$ does not exhibit the sharp yield point. The origin of this undulation is the smoothing of recorded curve only.

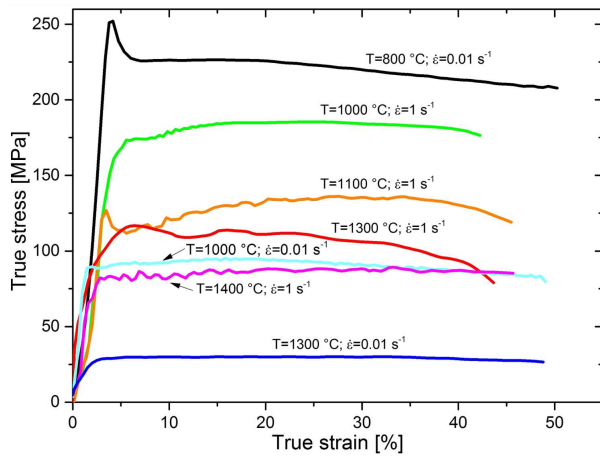


Fig. 1. Compression flow curves at various temperatures and strain rates.

Ultimate compressive strength (UCS) was determined from each flow curve. The temperature dependence of UCS is shown in Figure 2 for the $\dot{\epsilon} = 1 \text{ s}^{-1}$ and $\dot{\epsilon} = 0.01 \text{ s}^{-1}$. Fitted lines indicate that the slope is steeper for the $\dot{\epsilon} = 0.01 \text{ s}^{-1}$ than for $\dot{\epsilon} = 1 \text{ s}^{-1}$. The main reason of this difference is the sharp yield point of the sample deformed at $800 \text{ }^\circ\text{C}$. On the other hand, the slope between samples deformed at $1000 \text{ }^\circ\text{C}$ and $1300 \text{ }^\circ\text{C}$ is very similar to that at high strain rates. The strength of studied material at $\dot{\epsilon} = 1 \text{ s}^{-1}$ exceeds 170 MPa at $1000 \text{ }^\circ\text{C}$ and decreases below 100 MPa only at $1400 \text{ }^\circ\text{C}$. This behaviour is much different from that of Ti64 that has strength value at $1000 \text{ }^\circ\text{C}$ and $\dot{\epsilon} = 1 \text{ s}^{-1}$ already below 50 MPa [15] but similar to commercial stainless steel AISI 304 [16].

SEM observations revealed that porosity present in the cast condition was not completely removed by high temperature deformation. Two types of pores were found

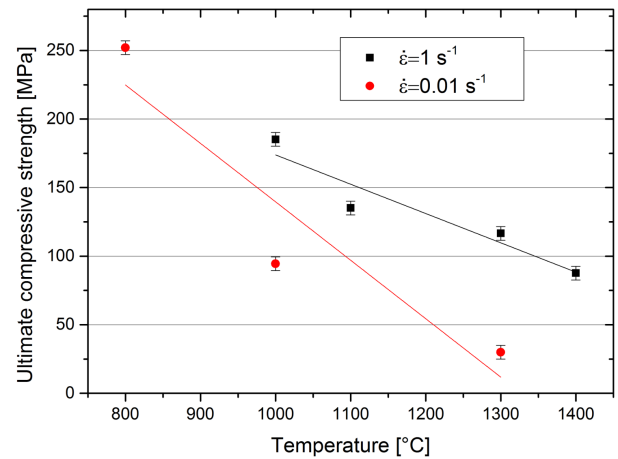


Fig. 2. The temperature dependence of the ultimate compressive strength for two strain rates.

in the deformed material: (i) small, homogeneously distributed pores and (ii) larger pores mainly along grain boundaries. Smaller pores of the size of a few micrometers were formed already during casting and Gleeble processing deformed the area around them and closed some of them. The deformed zones can be observed in backscattered electrons in Fig. 3a (sample deformed at $T = 1100 \text{ }^\circ\text{C}$ and $\dot{\epsilon} = 1 \text{ s}^{-1}$) as lighter area near both pores. The deformed area appears lighter in the SEM micrographs thanks to channelling contrast of the deformed crystal lattice that has locally different scattering condition. Larger pores have sizes of tens of micrometers and are located at the grain boundaries, especially in triple points, as in Fig. 3b for sample deformed at $T = 1300 \text{ }^\circ\text{C}$ and $\dot{\epsilon} = 1 \text{ s}^{-1}$. Note that these pores were not observed in all deformed samples and the correlation with temperature or strain rate of deformation is rather inconclusive.

EBSD measurements were performed to analyse the degree and the distribution of deformation present in samples. The area of $1300 \mu\text{m} \times 1800 \mu\text{m}$ and the step size of $4 \mu\text{m}$ were employed. For this purpose, kernel average misorientation (KAM) was determined for each data point as the mean misorientation of all points within the maximum distance of the triple step size around each point (note that hexagonal grid was used for measurements). Grain boundaries (points with misorientation higher than 5° from reference point) were excluded from each kernel. Example of inverse pole figure (IPF) map for sample deformed at $T = 1300 \text{ }^\circ\text{C}$ and $\dot{\epsilon} = 1 \text{ s}^{-1}$ is shown in Fig. 4a, corresponding KAM map is displayed together with the colour code of respective misorientations in Fig. 4b. It is clearly seen that the deformation (higher KAM value) is concentrated near the grain boundaries, especially near triple points. This phenomenon was present in all samples deformed at the strain rate $\dot{\epsilon} = 1 \text{ s}^{-1}$ and is typical in β -Ti deformed at high strain rates and/or relatively low temperatures [17].

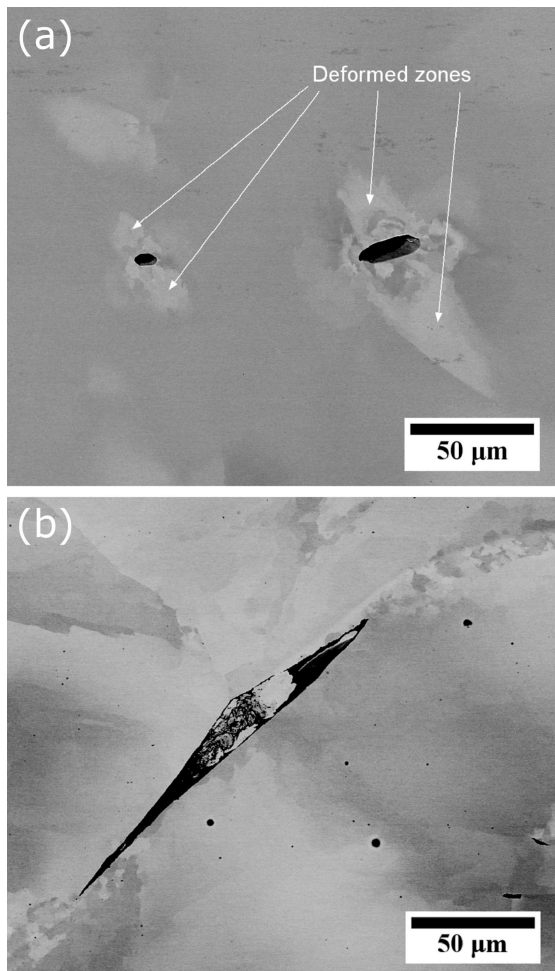


Fig. 3. (a) Small pores (formed during casting) in the sample deformed at $T = 1100\text{ °C}$ and $\dot{\epsilon} = 1\text{ s}^{-1}$, deformed zones are indicated by white arrows. (b) Large pore on grain boundary in sample deformed at $T = 1300\text{ °C}$ and $\dot{\epsilon} = 1\text{ s}^{-1}$, small black dots are remnants from polishing suspensions.

The KAM distribution of samples deformed at the lower strain rate of $\dot{\epsilon} = 0.01\text{ s}^{-1}$ depends strongly on the temperature of deformation. Figure 5a shows that at lowest temperature of 800 °C the KAM values are distributed very homogeneously while at higher temperature of 1000 °C (Fig. 5b), the deformation is concentrated at grain boundaries similarly as at the faster strain rate; *cf.* Fig. 4b. In addition, several spots of enhanced deformation (higher KAM value) can be seen in Fig. 5a. These spots indicate the presence of pores around which the material is highly deformed. The highest deformation temperature of 1300 °C leads to lowest amount of deformation which will be discussed below; *cf.* Fig. 5c. The area fraction of individual misorientations was computed from the KAM maps.

The respective KAM distributions for strain rates of $\dot{\epsilon} = 0.01\text{ s}^{-1}$ and $\dot{\epsilon} = 1\text{ s}^{-1}$ are shown in Fig. 6. At the $\dot{\epsilon} = 0.01\text{ s}^{-1}$, deformation stored in the material decreases with increasing temperature. The sample de-

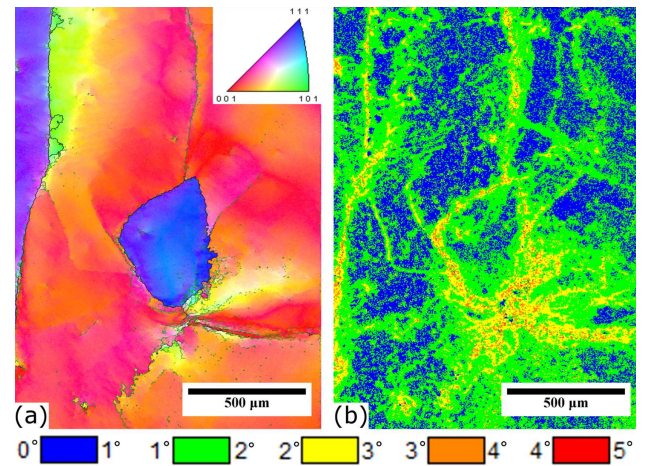


Fig. 4. Sample deformed at $T = 1300\text{ °C}$ and $\dot{\epsilon} = 1\text{ s}^{-1}$. (a) IPF map, (b) KAM map.

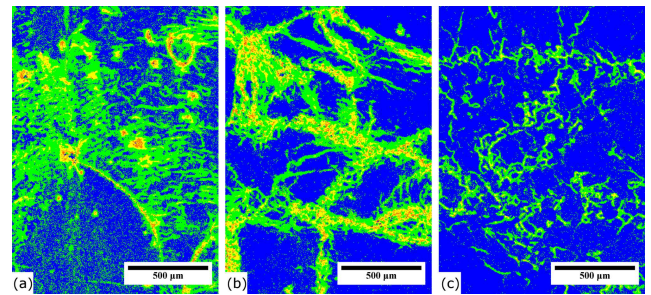


Fig. 5. KAM maps of samples deformed at $\dot{\epsilon} = 0.01\text{ s}^{-1}$ and (a) $T = 800\text{ °C}$, (b) $T = 1000\text{ °C}$ and (c) $T = 1300\text{ °C}$. For the orientation colour code, see Fig. 4.

formed at the highest temperature (1300 °C), contains almost 80% of area with KAM value less than 1° . At this slow strain rate, recovery processes are probably fast enough to reduce the dislocation density. The recovery rate increases with the increasing density. The recovery rate increases with the increasing temperature. Similar behaviour has been recently observed in other β -Ti alloy and was ascribed to high stacking fault energy of β -Ti [17] which enhanced the dynamic recovery and prevented the dynamic recrystallization. On the other hand, at the high strain rate $\dot{\epsilon} = 1\text{ s}^{-1}$, the deformation stored in material does not vary monotonously with increasing temperature. It increases up to 1100 °C , then decreases up to 1300 °C . As a consequence, one may assume that the effect of deformation temperature on the stored strain is only minor at the highest strain rate $\dot{\epsilon} = 1\text{ s}^{-1}$.

KAM analysis of EBSD data indicate that dynamic recovery occurs at the lower strain rates of $\dot{\epsilon} = 0.01\text{ s}^{-1}$ at the whole temperature range employed ($800\text{--}1300\text{ °C}$). On the other hand, even the highest temperature of 1300 °C was not high enough to initiate the recrystallization. In contrast, the stainless steel recrystallizes already at 900 °C to 1100 °C [16].

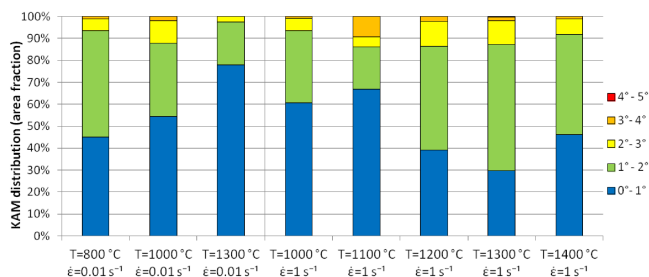


Fig. 6. Distribution of KAM values computed from each EBSD map as area fraction.

4. Conclusions

The mechanical properties of a biomedical alloy Ti–Nb–Zr–Ta–O were investigated at high temperatures and correlated with microstructure evolution. The following conclusion may be drawn from this experimental study:

- The deformation at elevated temperatures up to 1300 °C and the strain rate up to $\dot{\epsilon} = 1 \text{ s}^{-1}$ results in the dynamic recovery without any apparent recrystallization.
- The material is mostly deformed near grain boundaries and in the vicinity of pores formed already during casting.
- At the lower strain rate $\dot{\epsilon} = 0.01 \text{ s}^{-1}$ the deformation inside material drops with increasing temperature due to dynamic recovery.
- The minimum forming temperature of this alloy resulting in the strength comparable to that of Ti64 seems to be 1400 °C.

Acknowledgments

This work was financially supported by the Czech Science Foundation (project No. 17-20700Y) and by the joint project of the Ministry of Education, Youth and Sports of the Czech Republic (7AMB16AT012) and the Austrian Science Fund (FWF) (project No. I2391-N23). D.P. acknowledges financial support

by the Grant Agency of Charles University (project GAUK No. 1530217). M.J. and P.H. acknowledge partial financial support by ERDF under the project CZ.02.1.01/0.0/0.0/15_003/0000485.

References

- [1] H.J. Rack, J.I. Qazi, *Mater. Sci. Eng. C* **26**, 1269 (2006).
- [2] M. Geetha, A.K. Singh, R. Asokamani, A.K. Gogia, *Prog. Mater. Sci.* **54**, 397 (2009).
- [3] Y.T. Lee, G. Welsch, *Mater. Sci. Eng. A* **128**, 77 (1990).
- [4] J.-Y. Rho, T.Y. Tsui, G.M. Pharr, *Biomaterials* **18**, 1325 (1997).
- [5] M. Niinomi, *J. Mech. Behav. Biomed. Mater.* **1**, 30 (2008).
- [6] E. Eisenbarth, D. Velten, M. Müller, R. Thull, J. Brems, *Biomaterials* **25**, 5705 (2004).
- [7] A.T. Rack, *HJ Low modulus biocompatible titanium base alloys for medical devices*, United States Patent, 5,871,595, (1999).
- [8] J.I. Kim, H.Y. Kim, H. Hosoda, S. Miyazaki, *Mater. Trans.* **46**, 852 (2005).
- [9] M. Nakai, M. Niinomi, T. Akahori, H. Tsutsumi, M. Ogawa, *Mater. Trans.* **50**, 2716 (2009).
- [10] Q. Wei, L. Wang, Y. Fu, J. Qin, W. Lu, D. Zhang, *Mater. Des.* **32**, 2934 (2011).
- [11] M. Besse, P. Castany, T. Gloriant, *Acta Mater.* **59**, 5982 (2011).
- [12] J.I. Qazi, H.J. Rack, B. Marquardt, *JOM* **56**, 49 (2004).
- [13] J. Stráský, P. Hrcuba, K. Václavová, K. Horváth, M. Landa, O. Srba, M. Janeček, *J. Mech. Behav. Biomed. Mater.* **71**, 329 (2017).
- [14] D. Preisler, K. Václavová, J. Stráský, M. Janeček, P. Hrcuba, in: *METAL 2016, 25rd Int. Conf. on Metallurgy and Materials*, Ostrava Tanger Ltd, 2016, p. 1509.
- [15] R. Pederson, R. Gaddam, M.-L. Antti, *Cent. Eur. J. Eng.* **2**, 347 (2012).
- [16] S.-I. Kim, Y.-C. Yoo, *Mater. Sci. Eng. A* **311**, 108 (2001).
- [17] J. Zhao, J. Zhong, F. Yan, F. Chai, M. Dargusch, *J. Alloys Comp.* **710**, 616 (2017).